RSC Advances

PAPER

View Article Online
View Journal | View Issue

Cite this: *RSC Adv.*, 2023, **13**, 19770

Sophisticated and precise: design and implementation of a real-time optical detection system for ultra-fast PCR†

Bangchao Xi,[abc] Shaolei Huang,[abc] Yiquan An,[abc] Xianglian Gong,[abc] Jiayu Yang,[abc] Juntian Zeng,[abc] Shengxiang Ge*[abc] and Dongxu Zhang *[abc]

Quantitative Real-Time Polymerase Chain Reaction (qRT-PCR) has become indispensable in the realm of disease nucleic acid screening and diagnostics, owing to its remarkable precision and sensitivity, in which the real-time fluorescence detection system plays an extremely critical role. To solve the problems of long time and slow speed of traditional nucleic acid detection, PCR systems are evolving towards ultra-rapid configurations. Nonetheless, most extant ultra-rapid PCR systems either depend on endpoint detection for qualitative assessments due to inherent structural or heating constraints or circumvent the challenge of adapting optical systems to expeditious amplification systems, resulting in potential shortcomings in assay efficacy, volume, or expense. Consequently, this study proposed a design of a real-time fluorescence detection system for ultra-fast PCR, capable of executing six channels of real-time fluorescence detection. Through the meticulous calculation of the optical pathway within the optical detection module, effective regulation of system dimensions and the cost was accomplished. By devising an optical adaptation module, the signal-to-noise ratio was enhanced by approximately 307% without compromising the PCR temperature alteration rate. Ultimately, by employing a fluorescence model that accounted for the spatial attenuation effect of excitation light, as proposed herein, fluorescent dyes were arranged to evaluate the repeatability, channel interference, gradient linearity, and limit of detection of the system, which proved that the system had good optical detection performance. Finally, the real-time fluorescence detection of human cytomegalovirus (CMV) under 9 min ultra-fast amplification was achieved by a complete ultra-fast amplification experiment, which further validated the potential of the system to be applied to rapid clinical nucleic acid detection.

Received 20th May 2023
Accepted 21st June 2023

DOI: 10.1039/d3ra03363e

rsc.li/rsc-advances

Introduction

Nucleic acid testing is a molecular diagnostic technique that detects the structure or expression level of genetic material to make a relevant diagnosis. This technique boasts extensive applications in molecular biology, forensic science, clinical diagnostics, and biomedical research. Given the low concentration of initial samples, nucleic acid detection typically necessitates prior nucleic acid amplification. Quantitative Real-Time Polymerase Chain Reaction (qRT-PCR) serves as a paramount method for exponentially amplifying specific DNA fragments. In recent years, substantial outbreaks of infectious diseases, such as the novel coronavirus (2019-nCoV), African Swine Fever, and Monkeypox, have emerged, with qRT-PCR becoming a widely employed tool for nucleic acid screening and diagnosis, owing to its accuracy and heightened sensitivity.

Regrettably, current PCR instruments often demand 1–3 hours for assay completion and entail sizable, costly devices that necessitate specialized operators and professional environments. This undoubtedly constrains the deployment of such laboratory apparatuses in resource-limited settings. Over the past several decades, nucleic acid detection has progressively gravitated towards ultra-rapid methodologies, with researchers globally exploring ultra-fast PCR systems. Some scholars have performed ultra-fast PCR by water bath temperature variation,[1] Peltier control,[2] multi-temperature rotary,[3] or plasmonic photothermal heating. All these direct or indirect temperature regulation methods have to rely on endpoint detection for qualitative judgments due to the design of their structures or the effect of photothermal heating on real-time fluorescence.[4,5] However, real-time fluorescent quantitative PCR is indispensable for clinical applications, as simplistic ultra-fast PCR strategies fail to furnish reliable nucleic acid quantification results

[a]State Key Laboratory of Molecular Vaccinology and Molecular Diagnostic (Xiamen University), Xiamen 361102, Fujian, China. E-mail: zhangdongxu@xmu.edu.cn; sxge@xmu.edu.cn

[b]National Institute of Diagnostics and Vaccine Development in Infection Diseases (Xiamen University), Xiamen 361102, Fujian, China

[c]School of Public Health, Xiamen University, Xiamen 361102, Fujian, China

† Electronic supplementary information (ESI) available. See DOI: https://doi.org/10.1039/d3ra03363e

and gene copy number discrepancies, which are germane to patient condition evaluation, disease course monitoring, and prognosis assessment.[6]

To compensate, Cunha[7] *et al.* designed an ultra-fast PCR device that can complete 40 cycles of PCR in 10 min. The device uses a double-sided clamping amplification chamber with peltier for rapid temperature rise and fall, and an integrated fluorescence reader placed orthogonally to the amplification chip for real-time fluorescence detection; E. K. Wheeler[8] enables real-time PCR in less than 3 minutes by integrating a temperature conversion device and a fluorescence reader; T. Houssin[9] for rapid temperature rise and fall by means of a temperature controller and two heat exchangers with an integrated fluorescence reader for real-time detection; P. J. R. Roche[10] as well as S. Zhou[11] chose to use a dedicated PI camera for real-time fluorescence measurements in their respective studies. The majority of aforementioned studies have executed real-time fluorescence detection by incorporating external fluorescence readers or cameras. While this could accomplish rapid amplification detection, it circumvents the issue of adaptability between swift amplification systems and optical detection systems. Moreover, these studies lack tailored optical design and localized adjustments for ultra-fast configurations, potentially impacting fluorescence detection stability and detection limits. To some degree, this may result in excessively large and costly devices, ultimately compromising the instrument's overall portability.

Hence, a specially designed fluorescence detection module is not only instrumental in enhancing assay efficiency and the accessibility of diagnostic information but also significantly improves portability and cost reduction while maintaining the ultra-fast PCR system's performance. This enables swifter, more precise, and portable point-of-care testing (POCT).

In this study, we propose an ultra-fast PCR system based on multiple temperature zones. The system achieved the maximum heating and cooling rates of 24.12 °C s^{-1} and 25.28 °C s^{-1}, and was able to complete the nucleic acid amplification of human cytomegalovirus (CMV) within 9 min. And for the ultra-fast temperature changes brought about by the light collection structure, optical suitability, and system detection performance, a real-time fluorescence detection system design scheme is proposed. This solution can be used not only in the ultra-fast nucleic acid amplification system we designed but also as a reference for other nucleic acid amplification systems. The system is divided into two parts: the optical detection module and the amplification adaptation module; in the optical detection module, in order to achieve accurate control of the optical path, specific calculations, and simulations were performed to verify the optical path, and relevant component selection was carried out to achieve effective control of the system size and cost; in the amplification adaptation module, in order to enhance the fluorescence excitation efficiency while enabling ultra-fast amplification, a special structure was proposed in this study, and an optical surface was specially designed in combination with the temperature control module to substantially improve the signal-to-noise ratio of the system. In the subsequent study, the emission fluorescence due to the spatial attenuation effect of the excitation light is also modeled for specific concentrations, which has generalized implications for optical system performance testing experiments. Next, the performance of the optical system was verified for repeatability, channel crosstalk, gradient linearity, and limit of detection, and compared with the BioRad commercial PCR instrument to demonstrate the good optical detection performance of the system. Finally, sample amplification experiments were performed using human cytomegalovirus (CMV), showing good ultra-fast amplification as well as real-time fluorescence detection.

Materials and methods

System design and instrumentation

Ultra-fast temperature control module design. The physical diagram of the ultra-fast PCR system is shown in Fig. 1, which contains two key components: an ultra-fast temperature control module for PCR thermal cycling and a real-time fluorescence detection system, which is divided into two parts: an optical detection module and an optical adaptation module.[12] The overall size of the ultra-fast temperature control module is 140 mm × 130 mm × 70 mm, and it is used to obtain the temperature required for PCR by driving the PCR tube to move cyclically between multiple temperature zones. By introducing a control method for over-raising the temperature difference between the biological reagents in the PCR tube and the external heat source, *i.e.*, the introduction of a temperature over-regulation temperature zone, substantially increases the heat transfer rate between the reagent liquids, resulting in rapid PCR thermal cycling, which can complete 40 cycles of amplification in 9 minutes. Each temperature zone unit consists of an upper and lower symmetrical structure, including heat-

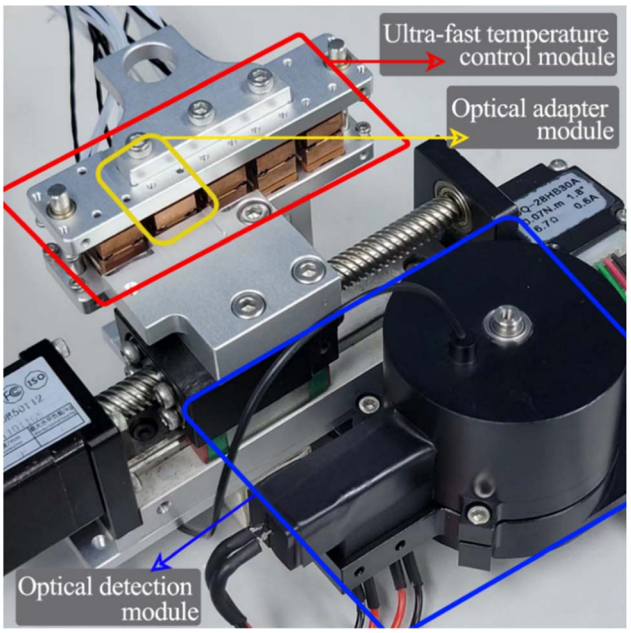

Fig. 1 Overall physical picture of the ultra fast PCR system.

generating pieces, heat-conducting pieces, heat insulating-pieces, and temperature sensors. The heat-conducting pieces are made of aluminum with good thermal conductivity to achieve temperature homogenization, and the pieces is made of a ceramic heater with the size of 10 mm × 10 mm × 1 mm (Tritech, Guangzhou). The horizontal movement of the PCR reaction tube is completed by servo control of the motor to achieve switching in different temperature zones. A more detailed description can be found in our previous work.[13,14,33]

Optical detection module design. The optical detection module consists of a full-spectrum light source cassette and six "bullet-shaped" optical channel cassettes integrated into a disc. The size of the full-spectrum light source box is 14 mm × 35 mm × 26 mm, and the optical channel box is a cylinder of φ = 52 mm and h = 40 mm after integration. Due to the different number of detection targets required for different diseases and the lack of detection scalability of a single channel, the optical detection module designed in this study can complete six channels of fluorescence detection, which has great potential for detection.[15–17]

Each channel of the optical channel box consists of the following parts. In order to eliminate the influence of stray light on the detection performance as much as possible, excitation filters with φ = 8 mm (United Optical, Beijing, China) and emission filters with φ = 10 mm (United Optical, Beijing, China) were selected. The dichroic mirror (Jinyi Optics, Beijing, China) with φ = 10 mm and the plano-convex lens with f = 10 mm, φ = 8 mm were selected, and the optical fiber and the photodiode were fixed, and the channel switching was completed by the rotation of the motor, which greatly reduced the overall size. The internal design of the channel box is chosen to use confocal optical path design in order to avoid the interference of excitation light to the maximum extent, as shown in Fig. 2(b), and the selection of each channel is shown in Table 1. The operating schematic of one of the optical channel boxes is shown in Fig. 3(b).

Table 1 Channel Selection

Channel	Excitation filter	Emission Filters	Dichroic mirror
Atto	436 ± 10 mm	455 ± 10 mm	DM 435/455
FAM	470 ± 15 mm	525 ± 10 mm	DM 470/525
HEX	520 ± 10 mm	571 ± 1 mm	DM 520/571
ROX	571 ± 10 mm	602 ± 10 mm	DM 571/602
CY5	635 ± 12.5 mm	681 ± 5 mm	DM 635/681
Quasar 705	680 ± 10 mm	710 ± 10 nm	DM 680/710

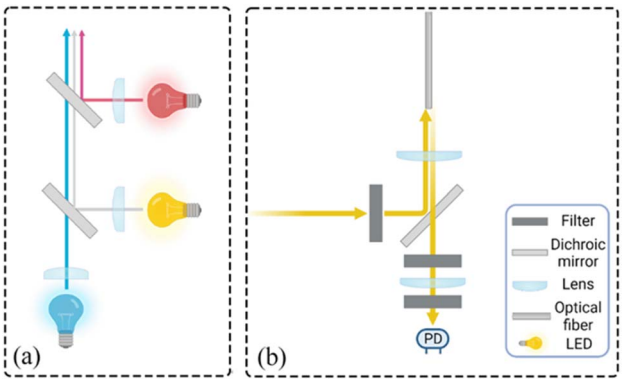

Fig. 3 Schematic diagram of the optical detection module (a) schematic diagram of the operation of the light source box (b) schematic diagram of the operation of the optical channel box.

In order to meet the requirement of stable excitation beam intensity and monochromatic luminescence spectrum, we choose Light Emitting Diode (LED) as the excitation light source. Three LEDs are integrated into the light source box to reduce the overall size of the system, which are blue, red and white LEDs. The light source box emits parallel light without high voltage power supply, and the overall size is 39 mm × 26 mm × 14 mm, as shown in Fig. 2(c). This compact design

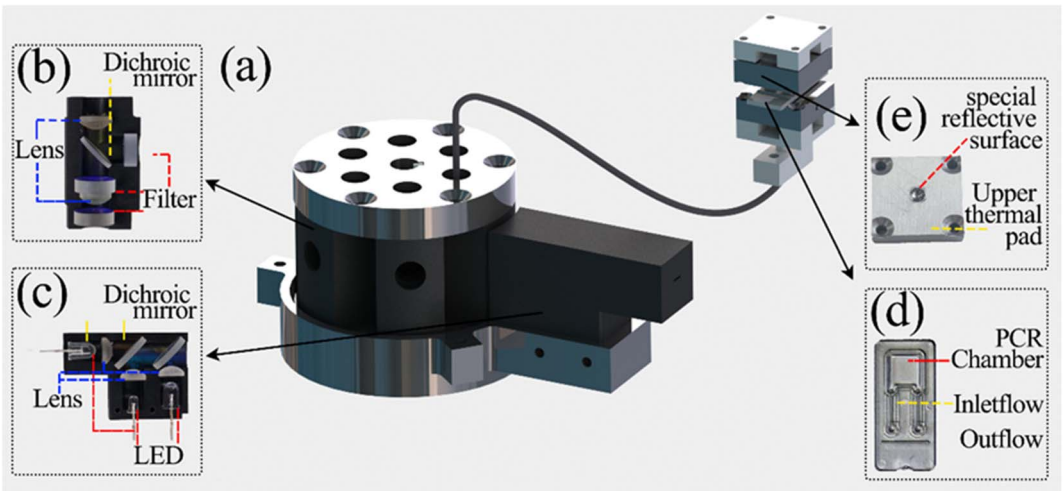

Fig. 2 Overall structure of the optical detection module (a) general view of the optical detection module (without housing); (b) internal structure of the "clip-like" optical channel cassette; (c) internal structure of the full-spectrum light source cassette; (d) physical view of the PCR reaction tube; (e) structure of the special heating sheet in the optical adaptation module.

Table 2 Selection of each component

Component Name	Company	Model
Plano-convex lens	Hengxiao optoelectronics, Nanjing	Customized
Optic fiber	Hecho, Nanjing	Customized
Photodiodes	Hamamatsu, Japan	S1133-01
Blue LED	Nichia, Japan	NSPB510BS
Red LED	Nichia, Japan	NSPR510GS
White LED	Nichia, Japan	NSDL510GS
Light source box dichroic mirror	Thorlabs, United States	DMLP605T DMSP505T

not only improves the integration of the excitation light source, but also helps to realize the portability of the real-time fluorescence detection system.[18,19] The light emitted from the LED can obtain the horizontal excitation light after the collimation of the plano-convex lens, and split by the dichroic mirror, finally forming a parallel, uniform outgoing light, incident light source channel box to complete the excitation of the detection channel, and its working principle diagram is shown in Fig. 3(a). The optical detection module is connected to the optical adaptation module by a $\varphi = 1.2$ mm optical fiber. In order to ensure a certain bending capacity using plastic multimode fiber, the selection of each component and the manufacturing company are shown in Table 2. A more visual understanding of the system can be obtained by referring to the attached video of the complete system in operation.

Optical adaptation module design. Due to the structural limitations imposed by the rapid temperature change of the solution, the amplification chamber of the PCR tube is designed in a flat shape to achieve rapid temperature change. The amplification chamber size is 4.5 mm × 4.5 mm × 1 mm, and the amplification chamber is flanked by 0.05 mm transparent polycarbonate films, as shown in Fig. 2(d). This also leads to a narrow location for real-time fluorescence detection in the upper and lower clamping "sandwich" heating structure, which is not easy to install detection devices, and the side of the light signal will be blocked by the heat-conducting sheet, making it difficult to collect. However, for the real-time fluorescence PCR instrument, good emission light collection is essential to obtain accurate quantitative diagnostic results.

Therefore, the fluorescence acquisition system is partially integrated into the temperature control system in this study, and a special optical reflective surface is innovatively designed on the heating sheet to enhance the overall performance of optical detection without affecting[20–22] the rapid temperature change. In the optical adaptation module, we discarded the commonly used side light harvesting method and chose to insert an optical fiber by punching a small hole of $\varphi = 1.2$ mm at the bottom of the thermal conductivity sheet where the 55° temperature zone is located. Due to the large size difference between the optical fiber and the amplification cavity, only a very small portion of the fluorescence of $\varphi = 1.2$ mm was excited by direct incidence. Therefore, how to make full use of the optical reflection to excite more fluorescence is of great significance to enhance the collection of useful signals as well as the signal-to-noise ratio.

In this study, an optical surface with special curved reflective properties is designed to achieve the full utilization of excitation light while avoiding excessive heat loss that may affect the ramp rate of the solution. While ensuring the reflective properties of the optical surface, the surface size should be moderate to avoid affecting the temperature change rate. The specific entity is shown in Fig. 2(e), and the specific key parameters will be explained in detail later. The excitation light excites the solution in the amplification cavity twice by direct incidence and reflection through the special curved surface of the upper thermal conductivity sheet, which significantly improves the fluorescence excitation efficiency. Since the fluorescence itself is a Lambertian light source, more fluorescence is reflected back into the fiber, which increases the total amount of fluorescence collected and improves the overall signal-to-noise ratio.

Control system design. As shown in Fig. 4, the block diagram of the control unit of the system shows the overall control and processing process. We chose STM32 as the main controller and focused on the following main functional modules according to the actual control requirements: (1) power supply module: responsible for voltage conversion and power supply for the sub-circuit; (2) LED driver circuit: to achieve constant current drive control of the excitation light source; (3) stepper motor driver circuit: to complete the drive control of the motor in the switching device to achieve channel switching; (4) communication module: used to communicate with the host computer and print debugging information as a circuit debugging interface; (5) signal conditioning and sampling circuit: to realize the conditioning and sampling of the output electrical signal of the photoelectric converter. In order to reduce the resistance value of the feedback resistor without affecting the conversion and detection of the fluorescent signal, this paper uses a T-shaped resistive feedback network instead of a single feedback

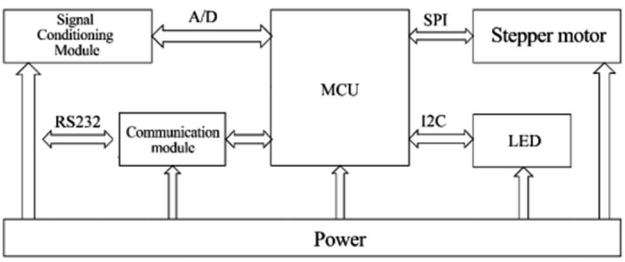

Fig. 4 Control system hardware structure block diagram.

resistor in the form of an optimized design. The photocurrent of sample fluorescence after photoelectric conversion is usually at the pA level. To accurately achieve the measurement of photocurrent, this system uses a precision *trans*-impedance amplifier (OPA380, Texas Instruments TI, USA). After the optical signal passed through the multiplexed selector switch composed of ADG1408, we designed a secondary amplifier circuit using TI's OPA277 operational amplifier to further amplify and process the optical signal.

Calculation of key parameters

Optical detection module optical path quantitative calculation. In the optical detection module, precise quantitative control of the optical path can maximize the signal-to-noise ratio and reduce the overall size of the module. In this study, the core optical components of each channel are integrated into an optical channel box, and the distance of each component in the optical path is further reduced through the calculation of the actual optical path, and the spot size is precisely controlled. Take the optical channel box of optical fiber collecting fluorescence incident optical channel as an example, the angle of optical fiber emission is determined, and the fluorescence passes through the lens to form a spot of the suitable size to be incident on the filter. Assume that the distance L from the exit point A to the vertex O of the lens sphere, the refractive indices n and $'$ of the air and lens, the radius of curvature r of the lens and the divergence angle U of the fiber are known (Fig. 5).

In ΔAEB, there are

$$\sin \alpha = (L - r) \times \frac{\sin U}{r} \tag{1}$$

$$\sin \alpha' = \sin \alpha \times \frac{n}{n'} \tag{2}$$

In ΔA′EB, there are

$$\frac{\sin \alpha'}{L' - r} = \frac{\sin U'}{r} \tag{3}$$

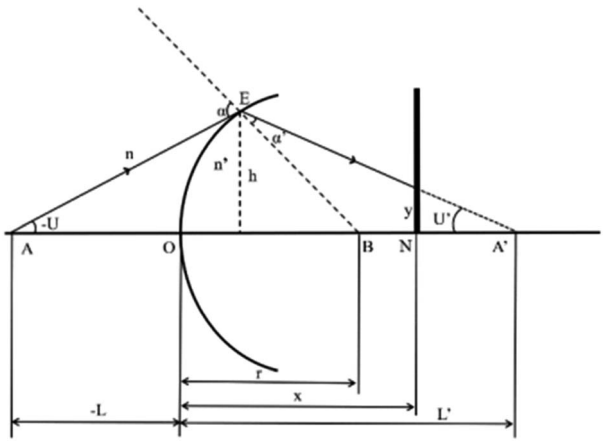

Fig. 5 Schematic diagram of light passing through optical components.

Therefore,

$$L' = r\left(\frac{\sin \alpha'}{\sin U'} + 1\right) \tag{4}$$

where

$$U' = U + \alpha - \alpha' \tag{5}$$

The filter is placed on the back side of the lens that is placed in the N point, set the ON distance x, the spot size y can be expressed as

$$y = (L' - x) \times \tan U' \tag{6}$$

The final result is

$$y = \left[r\left(\frac{\frac{n}{n'}\sin \alpha}{\sin U + \alpha - \arcsin\left(\frac{n}{n'}\sin \alpha\right)} + 1\right) - x\right] \times \tan\left[U + \alpha - \arcsin\left(\frac{n}{n'}\sin \alpha\right)\right] \tag{7}$$

By adjusting the radius of curvature $r$of the lens and the spacing x between the lens and the filter, the desired size of the light spot can be formed. Analogous calculations are also performed in the subsequent optical path, which can provide precise quantitative control of each level of the optical path and guide the overall selection of the instrument to reduce the size and improve the signal-to-noise ratio. The specific distances between the final components are shown in Table 3.

Optical adaptation module quantitative calculation. The excitation light is emitted through the optical fiber, reflected by the special reflective surface of the upper heat-conducting sheet, and then laid flat on the amplification cavity of the microfluidic chip to excite more fluorescent material and enhance the overall signal-to-noise ratio. The basic schematic of the reflective surface is shown in Fig. 6.

We divide the luminous flux of light source into equal amounts of according to the angle. The light intensity distribution of the light source is

$$I = I_0 \cos(\theta) \tag{8}$$

where θ is the zenith angle in spherical coordinates. Then integrating the relation between light intensity and luminous flux, and considering the face shape as a rotationally symmetric structure, we get

$$\varphi = \int_{\theta_2}^{\theta_1} I \sin \theta \, d\theta \tag{9}$$

Since the luminous flux of the light source is divided equally into N parts, we get

$$\varphi_n = \frac{\varphi_{\text{total}}}{N} \tag{10}$$

After sorting, we can get

Table 3 Optical path distance parameter table

The distance between the excitation filter and the binomial color mirror	Distance between binomial mirror and lens 1	Distance between lens 1 and fiber	Distance between binomial color mirror and emission filter 1	Distance between the emission filter 1 and the lens 2	Distance between the lens 2 and the emission filter 2	Distance between the emission filter 2 and the photodetector
6.59 mm	4.90 mm	7.93 mm	6.33 mm	1 mm	1.38 mm	1.98 mm

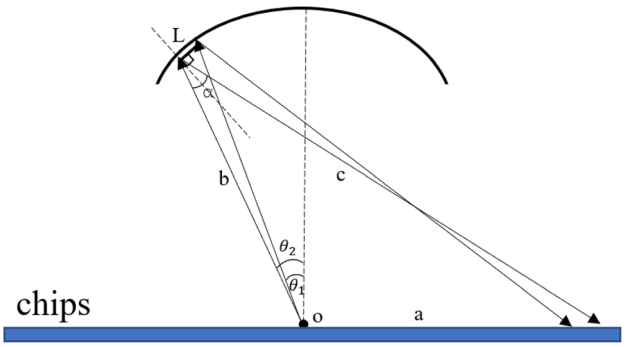

Fig. 6 Schematic diagram of the excitation light reflected by the special reflective surface of the upper heat-conducting sheet.

$$\varphi_n = \int_{\theta_n}^{\theta_{n+1}} I_0 \cos\theta \sin\theta \, d\theta \tag{11}$$

$$\varphi_n = \frac{1}{2} I_0 \left[\sin(\theta_{n+1})^2 - \sin(\theta_n)^2\right] \tag{12}$$

The final result is

$$\theta_{n+1} = \arcsin\sqrt{\frac{2\varphi_{\text{total}}}{NI_0} + \sin(\theta_n)^2} \tag{13}$$

On this basis, the target surface is also divided into N equal parts to establish the reflective surface, and the light source is linked to the target surface. In order to link the different θ angle intervals of the light source to the receiving surface ringband, the reflective surface is divided into multiple straight line segments L. The light from the light source should fall at the corresponding receiving surface after being reflected at the end point of the next reflective surface segment, and so on for subsequent reflective surface line segments. Since the incident fiber and the reflected ray are known, the next segment normal can be determined and thus the next segment is located in a straight line. Let the angle between the incident light and the reflected light is α, where b indicates the distance from the light source to the left end point of the next segment; c indicates the distance from the left end point of the next segment to the fall point of the light at the receiving surface; a indicates the distance from the LED to the fall point of the light at the receiving surface, which is obtained by the cosine theorem

$$\cos\alpha = \frac{b^2 + c^2 - a^2}{2bc} \tag{14}$$

Then, according to the next angle θ, the length of the current hypotenuse b as well as α, according to the law of cosines to solve the next section of the reflective surface length L.

$$\frac{L}{\sin(\theta_2 - \theta_1)} = \frac{b}{\sin\left(\frac{\pi}{2} - \alpha + \theta_1 - \theta_2\right)} \tag{15}$$

Based on the angle between the emitted ray and the next section of the reflecting surface and the positioning of the next section of the target surface, the rotation matrix is listed and the coordinates of the right endpoint of the next reflecting surface line segment are solved.

$$\begin{bmatrix} x_b \\ y_b \end{bmatrix} = \begin{bmatrix} \cos\theta & \sin\theta \\ -\sin\theta & \cos\theta \end{bmatrix} \begin{bmatrix} x_a \\ y_a \end{bmatrix} \tag{16}$$

The above iterative process is compiled using Matlab, the reflective surface bus data is solved, and the data is imported into Solidworks for 3D modeling. Machining adjustment using Unigraphics NX to perform surface machining (accuracy ±0.01 mm) on the surface of aluminum heating plates. And the surface is polished and painted to get the final product. A temperature sensor is installed on the back of the aluminum block to monitor the temperature zone and adjust the temperature profile in real time by computer to compensate for the heat loss caused by the absence of a heat-conducting sheet structure, to avoid a reduction in the expansion rate, and to effectively take into account the uniformity of the excitation light irradiation and the slowing down of the temperature rise caused by heat dissipation.

Results and discussion

Optical detection module optical path simulation

In this study, to ensure the overall light path design is sound, we use LightTools software to track the light propagation and evaluate the performance of the light path structure. The first is the simulation verification of the full-spectrum light source box, as shown in Fig. 7(a), the three LEDs emitted through the lens for collimation, respectively, and through the binomial color mirror for the initial split, the outgoing light parallel, uniform, and finally incident light source channel box to complete the excitation of the detection channel. The optical channel box is then simulated and verified, where the excitation light is incident in parallel, reflected by the binomial color mirror, and enters the fiber, as shown in Fig. 7(b). Light propagates in the fiber by total reflection, but due to dispersion, fiber bending,

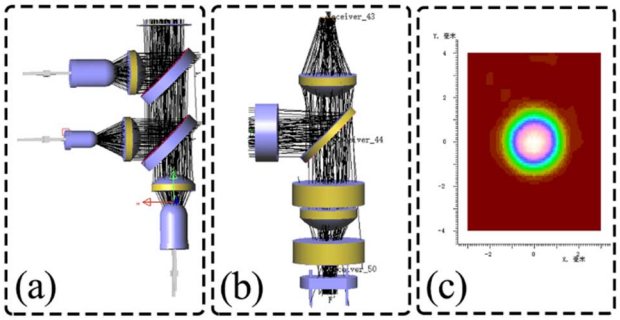

Fig. 7 Optical detection module optical path simulation (a) full-spectrum light source box simulation verification; (b) optical channel box simulation verification; (c) optical spot image at PD.

and other factors that make the propagation somewhat random, we replace the fiber with a circular detection surface and fluorescence emission surface with a radius comparable to the round end of the fiber cross-section. In the emission light path, the light source is set as Lambert light source to simulate the actual fluorescence emission,[23] and finally a circular spot with a diameter of 2.4 mm is formed to cover the PD window to complete the detection, as shown in Fig. 7(c). The final LightTools simulation results fine-tuned the actual calculation results, laying the foundation for the performance testing of the optical detection system and biological experimental testing.

Optical adaptation module simulation and experiment

In order to verify the performance of the optical adaptation module design and to investigate whether the application to ultra-fast conditions excites more fluorescence and improves the signal-to-noise ratio, the optical adaptation module

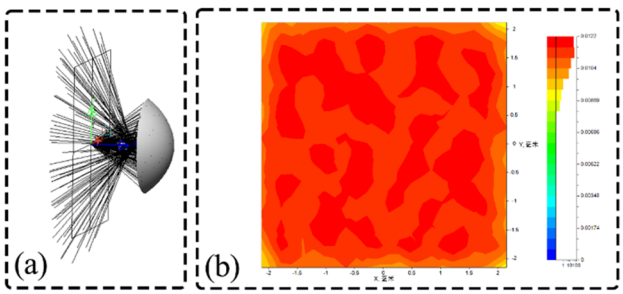

Fig. 8 Simulation of optical adaptation module (a) simulation of reflective surface of optical adaptation module; (b) final formation of light spot image.

reflective surface is simulated using LightTools, as shown in Fig. 8(a). After the excitation light is emitted, it is uniformly distributed in a square interval of 4.5 mm × 4.5 mm after being reflected by the calculated reflective base surface, and the formed light spot is shown in Fig. 8(b).

A comparison experiment was conducted between ordinary copper heat-generating pieces (the surface of which is blackened by oxidation due to rapid temperature changes), ordinary aluminum heat-generating pieces, and optically adapted heat-generating pieces with specially designed reflective surfaces to verify the performance of the adapted modules. The HEX channel was selected for the test experiment, DMSO was used as the blank control group, the HEX dye was diluted by 2 times, the appropriate concentration was selected, and the fluorescence values were read using the optical detection module, and the results of the test fluorescence values are shown in the table below (Table 4).

Comparison with the blank control group showed that the noise signal and the excitation light signal were not greatly increased by the addition of the optically adapted heating sheet, but the emission light signal was greatly increased. The signal-to-noise ratio, obtained by dividing the effective signal by the noise, is 307% higher than that of an ordinary copper heater and 203% higher than that of an ordinary aluminum heater, greatly improving the overall signal-to-noise ratio and detection capability of the instrument.

Fluorescence model considering the spatial decay effect of excitation light

Due to the absorption effect of fluorescent substances, the excitation light will be attenuated along the propagation direction during the propagation process, and this spatial attenuation effect leads to uneven distribution of fluorescence emission in space. The absorbance *versus* concentration deviates from linearity in highly concentrated solutions due to the limitation of the linear range of the Lambert–Beer law.[24–26] During fluorescence detection system performance testing, gradient stability and linearity are often screened, and such deviations can introduce a certain amount of error during final instrument performance verification. To this end, we conducted tests based on the FAM channel, studied the spatial intensity distribution of fluorescence emission over a wide concentration range, obtained the relationship between the received fluorescence intensity and the concentration of fluorescent substances, and established a fluorescence model that includes the spatial attenuation effect to avoid similar spatial attenuation problems in subsequent experiments and reduce misjudgment of the instrument performance.

Table 4 Comparison of the effect of optically adapted reflective surfaces

	Ordinary copper heat-generating pieces	Ordinary aluminum heat-generating pieces	optically adapted heat-generating pieces
Blank	2391.1	2406.2	2417.8
Gradient 4 (15 ug ml^{-1})	24 500.2	34 508.2	65 343.2
Valid signals	22 109	32 117.2	62 952.2

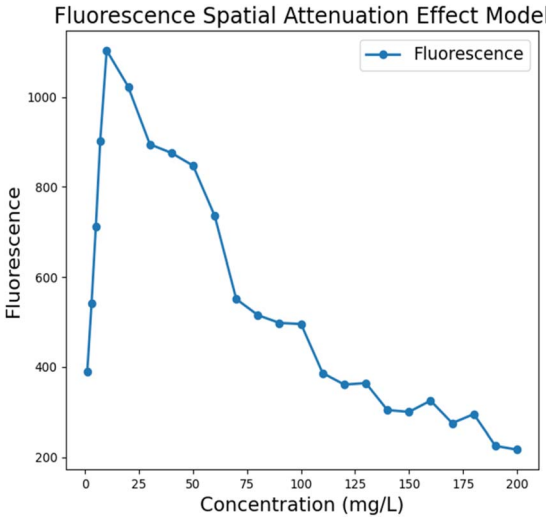

Fig. 9 Fluorescence modeling results considering the spatial attenuation effect of excitation light.

We performed fluorescence value acquisition and averaging based on a BioRad commercial PCR instrument using the organic solvent dimethyl sulfoxide (DMSO) formulated with a fluorescent dye for the FAM (fluorescein isothiocyanate) channel at concentrations from 1 mg L^{-1} to 200 mg L^{-1}. The following model between fluorescence intensity and concentration was obtained after deducting the noise signal. The results showed that the received fluorescence intensity showed an overall phenomenon of increasing and then decreasing, with an approximately linear increase at c < 20 mg L^{-1}. The spatial decay effect began to appear at c > 20 mg L^{-1}, and the fluorescence intensity did not increase with increasing concentration but weakened. The reason for this phenomenon may be that, limited by the linear range of Lambert–Beer law, the absorbance of the solution cannot maintain a completely positive correlation with the solution concentration when the concentration is higher than a certain range, and the spatial attenuation effect of the excitation light in the high concentration solution becomes significant. In the ultra-fast PCR assay, the initial viral amount of the pathogen is difficult to reach too high a concentration range even after multiple rounds of amplification, which also circumvents the effect of spatial decay on the instrument performance measurement to a certain extent (Fig. 9).

Overall system performance verification

Repeatability testing. The optical adaptation module designed in this paper is integrated with the optical detection module to form a real-time fluorescence detection system, and the overall performance is tested. The reproducibility of the system was first tested by testing the coefficient of variation (CV) of each channel at different concentrations of fluorescent dye samples. For this purpose, three test fluorescent dyes, FAM (fluorescein isothiocyanate), HEX (6-HEX, SE), and ROX (R4526), were prepared using the organic solvent dimethyl sulfoxide (DMSO) and diluted in a 2-fold gradient to obtain high, medium, and low concentrations of 10 mg L^{-1}, 0.1 mg L^{-1}, and 0.001 mg L^{-1} of the fluorescent dyes, respectively. Subsequently, 20 μL of each concentration of fluorescent dye was taken and added to the PCR reaction tubes, and 500 consecutive fluorescence measurements were performed. The results are shown in Table 5: the detection CV values of all samples for each channel were less than 0.2%, where the maximum value was 0.197% and the minimum value was 0.015%. This result indicates that the system has good detection repeatability and stability during fluorescence detection, and can effectively avoid data fluctuation caused by error interference during the detection process. It is of great significance to ensure accurate and rapid nucleic acid detection and provides a solid foundation for the rest of the performance tests and biological experiments.

Table 5 Fluorescent dye detection repeatability test results

Dye	Concentration	CV (%)
FAM	High	0.053
	Moderate	0.107
	Low	0.197
ROX	High	0.015
	Moderate	0.053
	Low	0.098
HEX	High	0.047
	Moderate	0.098
	Low	0.166

Channel crosstalk test. In multi-channel real-time fluorescence quantitation, the crosstalk between channels is a problem that cannot be ignored. Due to the partial overlap of the excitation and fluorescence spectra between different channels, mechanical structure leakage, circuit noise, and other factors, there is a certain degree of channel crosstalk in the detection. In order to have a deeper understanding of the fluorescence crosstalk of this system, we conducted a channel crosstalk experiment. In our experiments, we used three channels of excitation light to excite each channel and its corresponding dye and recorded the sampled fluorescence values in the corresponding excitation states. In addition, we used ultrapure water as a control group. As shown in Fig. 10, the channel crosstalk data are presented in the form of a three-dimensional bar graph.[31] As can be seen from the figure, the fluorescent dye only generates high fluorescence intensity when the corresponding channel is excited, and the fluorescence generated by the rest of the channels does not exceed 10% of the fluorescence intensity generated by the corresponding channel, and the fluorescence signal feedback of ultrapure water CK in each channel is also at a very low level, which verifies the feasibility of the system in multiplex detection. The inter-channel crosstalk problem will be further solved by the algorithm later.

Gradient linearity test. For nucleic acid detection instruments, the detection gradient is the relationship between the nucleic acid concentration or copies and the detection signal within a certain range.[32] The linear relationship allows the nucleic acid detection instrument to infer the nucleic acid concentration or copy number in the sample based on the

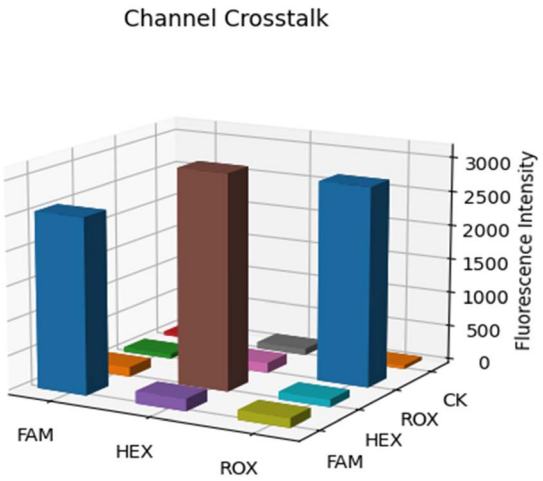

Fig. 10 Three-dimensional histogram of channel crosstalk data.

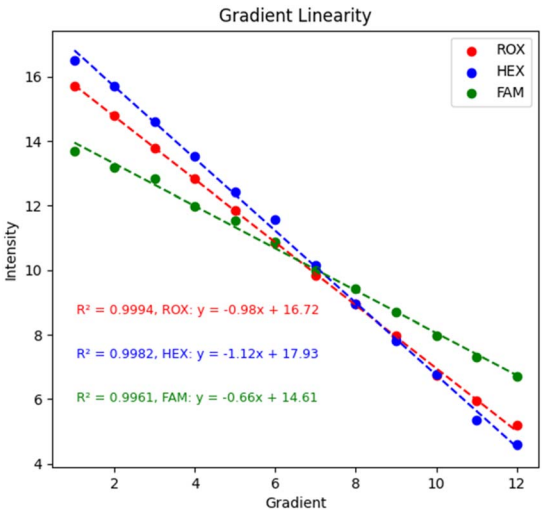

Fig. 11 System gradient linearity.

detection signal. It is critical for quantitative analysis in research and for viral load assessment in diagnostic processes, among others. In this study, DMSO was used to dilute the FAM, HEXand ROX dyes in a 2-fold gradient. With the fluorescence model of the spatial decay effect of excitation light, the concentration range should not be too large or it will lead to misjudgment of performance. Finally, DMSO was used as a blank control group for gradient testing, and the final results are shown in Fig. 11. Each of the three channels was tested with 12 gradients, and 100 data were collected for each gradient and averaged, and the values were normalized by subtracting the blank control group using the LOG function with a base of 2. The values of each channel were above 0.99, which had good linearity and established the basis for subsequent biological experiments.

Limit of detection test. The limit of detection (LOD) is the lowest nucleic acid concentration that can be detected by the instrument. For nucleic acid detection, the limit of detection is

Table 6 Comparison of limit of detection of FAM channels

Concentration (ng mL^{-1})	Ultrafast PCR real-time fluorescence detection system – FAM channel		Bio-rad PCR instrument – FAM channel	
	$y + 3\sigma$	S/N	$y + 3\sigma$	S/N
24.41	9482.77 + 19.81	57.13	2387.33 + 7.07	20.49
12.21	8849.53 + 20.24	31.79	2282.67 + 2.83	13.01
6.103	8368.27 + 14.29	15.78	2248.83 + 3.74	3.28
3.02	8200.40 + 20.77	6.48	2238.33 + 3.74	0.97
1.51	8112.23 + 19.44	3.25	2232 + 6.16	−0.21
0.76	8052.30 + 17.52	0.92	2202 + 2.45	−9.24
Blank	8030.60 + 15.93		2234 + 2.45	

Table 7 Comparison of limit of detection of HEX channels

Concentration (ng mL^{-1})	Ultrafast PCR real-time fluorescence detection system – HEX channel		Bio-rad PCR instrument – HEX channel	
	$y + 3\sigma$	S/N	$y + 3\sigma$	S/N
7.32	4514.83 + 15.65	9.73	2092 + 2.45	23.92
3.66	4462.5 + 17.28	6.83	2049.16 + 2.44	16.07
1.83	4413.56 + 18.75	4.39	2004.83 + 6.16	5.50
0.92	4383.03 + 15.39	3.47	1987 + 4.89	3.75
0.46	4353.33 + 19.76	1.74	1969 + 6.48	0.98
0.23	4340.36 + 23.81	0.97	1960.33 + 1.41	−0.13
Blank	4311.2 + 13.88		1961 + 4.89	

of great significance because it directly affects the overall sensitivity and accuracy of the instrument, which is critical in the detection of early viral infections or trace nucleic acids. Here, DMSO was still used to dilute FAM, HEX, and ROX master mixes in a 2-fold gradient. The spatial decay effect fluorescence model of excitation light shows that the measurement range cannot be too large, so the mother liquor concentrations were set to 100 ug mL^{-1}, 15 ug mL^{-1} and 5 ug mL^{-1}, respectively. After the three fluorescent dyes were added to the microfluidic chip chamber, fluorescence excitation, and acquisition were performed using the corresponding channels for the samples to be tested. To further characterize the performance of the system, a control experiment was conducted using

Table 8 Comparison of limit of detection of ROX channels

Concentration (ng mL^{-1})	Ultrafast PCR real-time fluorescence detection system – ROX channel		Bio-rad PCR instrument – ROX channel	
	$y + 3\sigma$	S/N	$y + 3\sigma$	S/N
9.77	1297.03 + 1.67	10.10	3348.33 + 1.41	343.92
4.88	1241.03 + 3.75	3.01	2545.33 + 9.90	54.11
2.44	1231.67 + 4.90	1.87	2192.67 + 6.16	30.51
1.22	1224.20 + 2.49	1.29	2043.33 + 5.10	11.17
0.61	1223.33 + 1.41	1.26	1996.67 + 3.74	4.54
0.31	1220 + 2.45	0.81	1976.67 + 3.74	0.76
Blank	1213 + 6.481		1972.67 + 4.89	

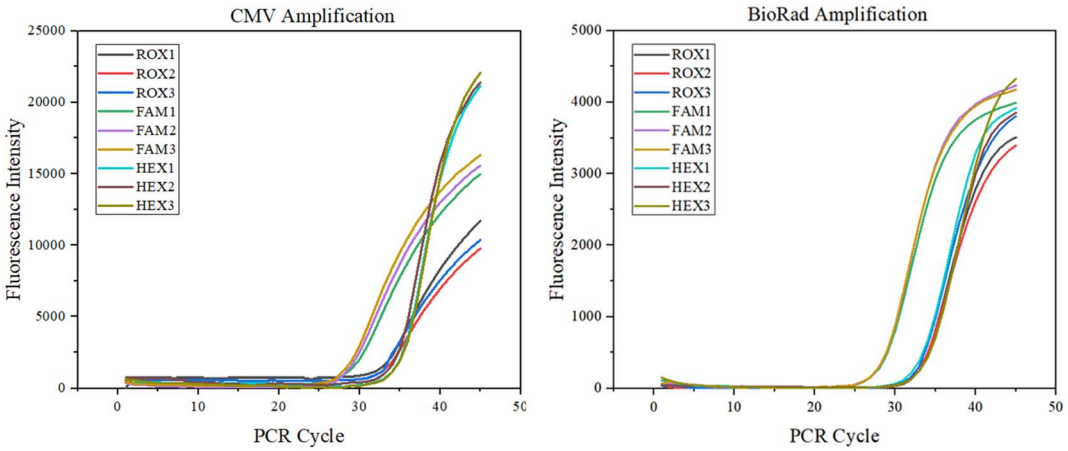

Fig. 12 CMV amplification experiments.

a commercial PCR instrument from BioRad, with the amplification program set to maintain 25° for light collection, and six sets of experiments were performed for each gradient. Afterward, 150 replicates of each gradient were tested using this system, and the mean value y was taken and the standard deviation σ was. The blanks were then read for DMSO to determine their mean y_{blank} and three standard deviations $3\sigma_{\text{blank}}$, and we defined LOD as the lowest concentration of the fluorophore-loaded solution with S/N greater than 1, where the signal and noise were calculated[27,28]

$$S = y - y_{\text{blank}} \tag{17}$$

$$N = \sqrt{(3\sigma)^2 + (3\sigma_{\text{blank}})^2} \tag{18}$$

The final results are shown in the following tables (Tables 6–8). The real-time fluorescence detection system has a good limit of detection, up to 1.51 ng ml^{-1} for the FAM channel, 0.46 ng ml^{-1} for the HEX channel, and 0.61 ng ml^{-1} for the ROX channel, with slightly better performance than the BioRad PCR instrument in the FAM and HEX channels, and basically the same performance as BioRad in the ROX channel, showing a better detection performance.

Nucleic acid amplification detection test. Combined with an ultra-fast elevation system, a final assessment of the system's potential for clinical application was performed. Amplification assays were performed with HCMV DNA with an amplified fragment of 120 bp. The viral DNA/RNA extraction kit (magnetic bead method, Genmagbio, Changzhou, China) was used to extract the HCMV strain AD169 from ARPE19 cell culture, which was diluted 16 times with 1× TE buffer and stored at −20 °C (Sangon Biotech, Shanghai, China). The virus was extracted from DNA and mixed with reagents to form an amplification system. The amplification system consisted of a 3.125 μL DNA template (35.2 ng μL^{-1}), 2.5 μL buffer, 0.625 μL 10 mM dNTPs, 0.625 μL forward primer, 0.625 μL reverse primer and 0.625 μL probe, 0.25 μL Taq-enzyme, and 7.25 μL DEPC.20 μL of the solution was added to the amplification chamber of the microfluidic chip, and then 5 μL of paraffin oil was added to block the channels of the microfluidic chip to prevent the solution from evaporating.[29,30] The final nucleic acid amplification experiment with 45 temperature cycles can be completed in 9 min. The corresponding fluorescence detection result curve is shown below, and compared with the BioRad commercial PCR instrument, which proves the value of the system applied to clinical rapid nucleic acid detection (Fig. 12).

Conclusions

In summation, we devised an innovative real-time fluorescence detection system capable of performing real-time fluorescence detection in ultra-fast PCR contexts. By integrating the fluorescence acquisition component with the temperature control system through optical design and ingeniously crafting a specialized optical reflective surface on the heat-generating elements, the signal-to-noise ratio was enhanced by approximately 307% without compromising the PCR temperature alteration rate. Concurrently, the amalgamation of meticulously calculated optical pathways ensured a precise system with controllable dimensions and cost. Ultimately, based on the fluorescence model accounting for the spatial decay effect of excitation light, we employed fluorescent dyes to validate the system's performance. The coefficient of variation (CV) for channel detection was below 0.2%; channel crosstalk did not surpass 10% of the corresponding channel's fluorescence intensity; the 12 gradient values exhibited excellent linearity, exceeding 0.99; the limit of detection for FAM and HEX channels slightly surpassed those of the BioRad PCR instrument, while the ROX channel's performance was essentially equivalent to that of BioRad. Lastly, the system successfully achieved real-time fluorescence detection within a 9 minute ultra-fast CMV amplification process, further substantiating the system's potential for expeditious clinical nucleic acid detection.

Conflicts of interest

There are no conflicts to declare.

Acknowledgements

This work was supported by grants from the National Natural Science Foundation of China (grant number 62003284), the Science and Technology Projects of Fujian Province (grant number 2021Y0093), the Science and Technology Projects of Xiamen City (grant number 35022022YJ05) and the Presidential research fund of Xiamen University (grant numbers 20720210089, 20720220005).

Notes and references

1 R. L. Nouwairi, L. L. Cunha, R. Turiello, *et al.*, Ultra-rapid real-time microfluidic RT-PCR instrument for nucleic acid analysis, *Lab Chip*, 2022, **22**(18), 3424–3435.
2 E. K. Wheeler, C. A. Hara, J. Frank, *et al.*, Under-three minute PCR: probing the limits of fast amplification, *Analyst*, 2011, **136**(18), 3707–3712.
3 J. H. ung, S. J. Choi, B. H. Park, *et al.*, Ultrafast rotary PCR system for multiple influenza viral RNA detection, *Lab Chip*, 2012, **12**(9), 1598–1600.
4 J. H. Son, B. Cho, S. G. Hong, *et al.*, Ultrafast photonic PCR, *Light: Sci. Appl.*, 2015, **4**(7), e280.
5 J. Cheong, H. Yu, C. Y. Lee, *et al.*, Fast detection of SARS-CoV-2 RNA via the integration of plasmonic thermocycling and fluorescence detection in a portable device, *Nat. Biomed. Eng.*, 2020, **4**(12), 1159–1167.
6 E. Pishbin, M. Eghbal, M. Navidbakhsh, *et al.*, Localized air-mediated heating method for isothermal and rapid thermal processing on lab-on-a-disk platforms, *Sens. Actuators, B*, 2019, **294**, 270–282.
7 R. L. Nouwairi, L. L. Cunha, R. Turiello, *et al.*, Ultra-rapid real-time microfluidic RT-PCR instrument for nucleic acid analysis, *Lab Chip*, 2022, **22**(18), 3424–3435.
8 E. K. Wheeler, C. A. Hara, J. Frank, *et al.*, Under-three minute PCR: probing the limits of fast amplification, *Analyst*, 2011, **136**(18), 3707–3712.
9 T. Houssin, J. Cramer, R. Grojsman, *et al.*, Ultrafast, sensitive and large-volume on-chip real-time PCR for the molecular diagnosis of bacterial and viral infections, *Lab Chip*, 2016, **16**(8), 1401–1411.
10 P. J. R. Roche, M. Najih, S. S. Lee, *et al.*, Real time plasmonic qPCR: how fast is ultra-fast? 30 cycles in 54 seconds, *Analyst*, 2017, **142**(10), 1746–1755.
11 S. Zhou, T. Gou, J. Hu, *et al.*, A highly integrated real-time digital PCR device for accurate DNA quantitative analysis, *Biosens. Bioelectron.*, 2019, **128**, 151–158.
12 Y. Peng, C. Lin, Y. Li, *et al.*, Identifying infectiousness of SARS-CoV-2 by ultra-sensitive SnS2 SERS biosensors with capillary effect, *Matter*, 2022, **5**(2), 694–709.
13 Y. Q. An, S. L. Huang, B. C. Xi, *et al.*, Ultrafast Microfluidic PCR Thermocycler for Nucleic Acid Amplification, *Micromachines*, 2023, **14**(3), 658.
14 S. Huang, J. Wu, H. Dai, R. Gao, H. Lin, D. Zhang and S. Ge, Development of amplification system for point-of-care test of nucleic acid, *Comput. Methods Biomech. Biomed. Eng.*, 2022, **25**(9), 961–970.
15 S. O'Driscoll, B. D. MacCraith and C. S. Burke, A novel camera phone-based platform for quantitative fluorescence sensing, *Anal. Methods*, 2013, **5**(8), 1904–1908.
16 T. Anazawa and M. Yamazaki, An ultra-small, multi-point, and multi-color photo-detection system with high sensitivity and high dynamic range, *Lab Chip*, 2017, **17**(24), 4231–4242.
17 M. Lehnert, E. Kipf, F. Schlenker, *et al.*, Fluorescence signal-to-noise optimisation for real-time PCR using universal reporter oligonucleotides, *Anal. Methods*, 2018, **10**(28), 3444–3454.
18 J. A. DuVall, D. Le Roux, A. C. Tsuei, *et al.*, A rotationally-driven polyethylene terephthalate microdevice with integrated reagent mixing for multiplexed PCR amplification of DNA, *Anal. Methods*, 2016, **8**(40), 7331–7340.
19 L. Zhu, C. Zhu, G. Deng, *et al.*, Rapid identification of H5 avian influenza virus in chicken throat swab specimens using microfluidic real-time RT-PCR, *Anal. Methods*, 2014, **6**(8), 2628–2632.
20 W. Chang, K. Zhou, Z. Wang, *et al.*, An analytical method for cold optical lens design based on LightTools, *AOPC 2021: Infrared Device and Infrared Technology*. SPIE, 2021, vol. 12061, pp. 448–454.
21 X. Yang, H. Gao, F. Qian, *et al.*, Internal standard method for the measurement of doxorubicin and daunorubicin by capillary electrophoresis with in-column double optical fiber LED-induced fluorescence detection, *J. Pharm. Biomed. Anal.*, 2016, **117**, 118–124.
22 Y. Ma, L. Zeng, and J. Zhang. A fluorescence detection optical system for real-time quantitative PCR, *Optical Design and Testing X*, International Society for Optics and Photonics, 2020, vol. 11548, p. 115481U.
23 B. L. Fernández-Carballo, C. McBeth, I. McGuiness, *et al.*, Continuous-flow, microfluidic, qRT-PCR system for RNA virus detection, *Anal. Bioanal. Chem.*, 2018, **410**, 33–43.
24 C.-F. Chen, J. H. Halford and D. M. Harmon, A sensitive portable fluorometer coupled with miniaturized integrating sphere, *Meas. Sci. Technol.*, 2019, **31**(1), 015204.
25 D. Xu, X. Jiang, T. Zou, *et al.*, A microfluidic system for rapid nucleic acid analysis based on real-time convective PCR at point-of-care testing, *Microfluid. Nanofluid.*, 2022, **26**(9), 69.
26 Y. Fu, M. Huang and W. Li, Spatial intensity distribution model of fluorescence emission considering the spatial attenuation effect of excitation light, *Opt. Express*, 2021, **29**(5), 6468–6480.
27 C. Chen, Fluorescence detection of fluorescein and SYBR green-stained DNA by reflective cavity-coupled fluorometer–A quantitative study, *Measurement*, 2020, **163**, 107946.
28 C.-F. Chen, J. H. Halford and D. M. Harmon, A sensitive portable fluorometer coupledwith miniaturized integrating sphere, *Meas. Sci. Technol.*, 2019, **31**(1), 015204.
29 Y. Liu, H. Pan, S. Zhao, L. Zhu, Z. Li and L. Zhang, Structural optimization design of TEC temperature control system formicrofluidic PCR, *Transducer Microsyst. Technol.*, 2013, **32**, 85–92.

30 M. Shibamura, S. Yamada, T. Yoshikawa, T. Inagaki, P. H. A. Nguyen, H. Fujii, S. Harada, S. Fukushi, A. Oka, M. Mizuguchi, *et al.*, Longitudinal Trends of Prevalence of Neutralizing Antibody against Human Cytomegalovirus over the Past 30 Years in Japanese Women, *Jpn. J. Infect. Dis.*, 2022, **75**, 496–503.
31 N. Gupta, S. Augustine, T. Narayan, *et al.*, Point-of-care PCR assays for COVID-19 detection, *Biosensors*, 2021, **11**(5), 141.
32 S. N. Rao, D. Manissero, V. R. Steele, *et al.*, A systematic review of the clinical utility of cycle threshold values in the context of COVID-19, *Infect. Dis. Ther.*, 2020, **9**(3), 573–586.
33 S. Huang, Y. An, B. Xi, *et al.*, Ultra-fast, sensitive and low-cost real-time PCR system for nucleic acid detection, *Lab Chip*, 2023, **23**(11), 2611–2622.